JOURNAL OF THEORETICAL AND APPLIED MECHANICS
63, 1, pp. 151-164, Warsaw 2025
https://doi.org/10.15632/jtam-pl/196984

LOAD TRANSFER LAW AND BEARING CAPACITY OF THE ANCHORAGE INTERFACE BASED ON A THREE-STAGE MODEL

Longfei Li, Xuebin Wang

College of Energy and Mining Engineering, Shandong University of Science and Technology, Qingdao, China

Tongbin Zhao*, Minglu Xing, Weiyao Guo, Yubao Zhang

College of Energy and Mining Engineering, Shandong University of Science and Technology, Qingdao, China, and State Key Laboratory of Mining Disaster Prevention and Control Co-founded by Shandong Province and the Ministry of Science and Technology, Shandong University of Science and Technology, Qingdao, China

corresponding author Tongbin Zhao, e-mail: 2863898939@qq.com

The shear stress constitutive equation of an anchorage interface element is established based on a three-stage model, and the expressions for the interface shear stress and axial force distribution evolution during the whole process of anchor drawing are derived theoretically. The parameters of the interface model are given through anchor pull-out tests. Then, the load transfer law and the bearing performance of the anchorage interface under different anchoring agents are calculated and analyzed. The calculation method of the ultimate bearing capacity of the anchorage interface is verified by supplementary tests, which can provide theoretical guidance for the bolt support design.

Keywords: constitutive model, anchor pull-out test, law of load transfer, interface bearing capacity

1. Introduction

The rockbolt support has been widely used in the roadway surrounding rock support engineering, because it can fully mobilize the strength and self-stabilizing ability of the surrounding rock (Zhao *et al.*, 2021; Yi *et al.*, 2020). In the engineering site, failure of the rockbolt support system will lead to serious instability and damage of the surrounding rock. Therefore, the analysis and evaluation of the bearing capacity of the rockbolt support system are of great significance for improving the support effect and reducing the failure risk of the rockbolt support system (Fan *et al.*, 2021).

In order to explore the failure mechanism of the rockbolt support system, researchers have conducted a large number of laboratory experiments and in situ tests. The research results show that failure of the rockbolt support system is mainly caused by interface debonding or rockbolt breaking (Li, 2010; Wang *et al.*, 2023; Kilic *et al.*, 2002). According to the results of rockbolt pull-out tests under different pull-out loads, Høien *et al.* (2021) classified failure mechanisms of the anchorage into three categories: debonding slip below the yield strength of the rockbolt, debonding slip between the yield load and ultimate load, and rockbolt breaking under the ultimate load; Liu *et al.* (2021) studied the failure mechanism of the anchorage interface through laboratory rockbolt pull-out tests, then divided the failure mode of the anchorage interface into the shear slip mode and shear expansion slip mode. Cao *et al.* (2014) found that the failure mode of the rockbolt system is closely related to the contact performance of the anchorage interface and the actual stress state of the material. Researches show that a high-quality anchorage interface bonding performance is an important part of the bolt support design. It is of great significance to improve the bearing capacity of the anchorage interface to ensure long-term effectiveness of the rockbolt support.

In order to further explore the relationship between mechanical parameters of the anchorage interface and anchorage bearing capacity, Kilic *et al.* (2002) conducted a series of laboratory tests on a grouting rockbolt, and put forward some empirical formulas for calculating the bearing capacity of the rockbolt. Holý (2017) used sandstone as an anchor matrix to carry out an anchor tensile test, and it was found that interfacial shear friction and surrounding rock properties had obvious influence on anchorage performance. Yahia *et al.* (1998) carried out a large number of tensile tests of rockbolts under different anchorage conditions, and found that the mechanical properties of anchoring agents affected the bearing capacity of the anchorage. A large number of experimental studies show that (Huang *et al.*, 2019; Wu *et al.*, 2019; Du *et al.*, 2021) the bond strength of the anchorage interface determines the critical shear stress when the anchorage interface is destroyed, and its deformation characteristics determine the load transfer mode and the distribution law of interfacial shear stress on the anchorage interface. Therefore, the shear stress-slip displacement relationship of the anchorage interface is the basis for studying deformation characteristics of the anchorage interface. A reasonable interface shear-slip model can effectively explain the interface load transfer and damage mechanism. The bond-slip models commonly used in the existing research to characterize the shear stress-shear displacement relationship of the anchorage interface are bilinear model (Cai *et al.*, 2004), trilinear model (Ma *et al.*, 2016; Nie *et al.*, 2019; Chen *et al.*, 2021) and nonlinear model (Nemcik *et al.*, 2014). According to the existing bond-slip model, many scholars have studied it by analytical and numerical methods (Chen *et al.*, 2020; Chen and Li, 2022; Yue *et al.*, 2022), which reveals the evolution law of shear stress distribution at the anchorage interface and provides a reference for the study of bearing capacity of the anchorage interface.

In summary, the bonding performance of the anchorage interface directly affects the bearing capacity of the anchorage, and the research on the influence rules of interface model parameters on the bonding performance of the anchorage interface still needs to be improved. Therefore, this paper deduces the load transfer law of the anchorage interface through theoretical derivation, carries out anchor rod pull-out tests under different anchoring conditions of anchoring agents, tests and analyzes the constitutive model parameters of the anchorage interface, and conducts in-depth research on the bearing capacity of the anchorage interface.

2. Analysis of load transfer laws at the anchorage interface

2.1. Three-stage interface element constitutive model and parameters

As shown in Fig. 1, the three-stage constitutive model divides the debonding failure process of the anchorage interface element into three stages: I – elastic stage: shear stress increases linearly with shear displacement. τ_s^d is the peak shear strength of the anchorage interface element in the elastic stage, and δ_s^d is the corresponding shear displacement; II – bond damage stage: shear stress decreases linearly with shear displacement. τ_s^s is the residual shear strength of the anchorage interface element, which is also the shear strength at the onset of slip; δ_s^s is the corresponding shear displacement at the onset of slip; III – frictional slip stage: in this stage, friction plays the dominant role, and the shear stress remains constant. In the figure, k_{ss} represents the elastic shear stiffness characterizing the evolution of shear stress with shear displacement in the elastic stage of the interface element $k_{ss} = \tau_s^d/\delta_s^d$.

As shown in Fig. 1, the constitutive equation for evolution of shear stress damage in the anchorage interface element characterized by the three-stage constitutive model is

$$\tau_s = \begin{cases} K_{OA}\delta_s & \delta_s \leqslant \delta_s^d \\ \tau_s^d + K_{AB}(\delta_s - \delta_s^d) & \delta_s^d \leqslant \delta_s \leqslant \delta_s^s \\ \tau_s^s & \delta_s^s \leqslant \delta_s \leqslant \delta_s^f \end{cases} \tag{2.1}$$

where $K_{OA} = k_{ss} = \tau_s^d/\delta_s^d$, $K_{AB} = (\tau_s^d - \tau_s^s)/(\delta_s^d - \delta_s^s)$.

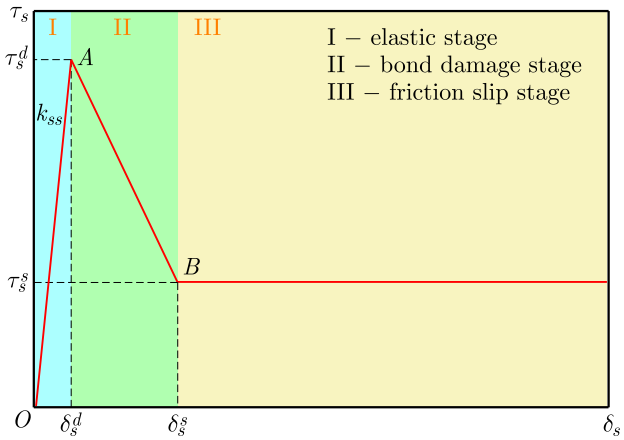

Fig. 1. Three-stage constitutive model and parameters

2.2. Load transfer equation for anchorage interface elements

As shown in Fig. 2a, to facilitate the analysis of load transfer laws at the anchorage interface, the shear interaction between the anchor rod and the rock mass is simplified into a spring contact model, with the side of the anchor rod connected to the rock mass through tangential line springs, the stiffness of which corresponds to the elastic shear stiffness of the anchorage interface.

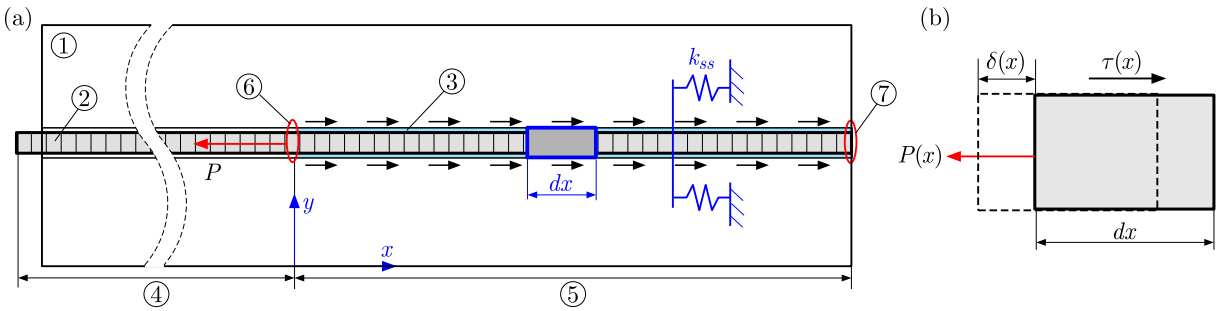

Fig. 2. Load transfer analysis diagram of the anchorage interface (1 – rock mass; 2 – anchor rod; 3 – anchor rod-rock mass coupling interface; 4 – free section of anchor rod; 5 – anchored section of anchor rod; 6 – anchored front end; 7 – anchored tail end): (a) simplified model of the anchorage interface, (b) anchorage interface element

Take an interface element at a distance of x from the anchored front end in the anchorage section. As shown in Fig. 2b, analyze the element using the load transfer method to determine the force equilibrium equations. The force equilibrium equations are

$$dP(x) = -2\pi r_b \tau(x)\, dx \qquad \frac{d\delta(x)}{dx} = -\frac{1}{\pi r_b^2 E_b} P(x) \tag{2.2}$$

where $P(x)$ is the axial force of the anchor rod at a distance x from the anchored front end, $\tau(x)$ is the shear stress, $\delta(x)$ is the shear displacement, r_b is the radius of the anchor rod, E_b is the elastic modulus of the anchor rod.

Substituting Eq. $(2.2)_1$ into Eq. $(2.2)_2$, the basic load transfer equation for the interface element is obtained

$$\frac{d^2\delta(x)}{dx^2} = \frac{2}{r_b E_b}\tau(x) \tag{2.3}$$

Substituting Eq. $(2.2)_2$ into Eq. (2.1), the differential equation for load transfer during the debonding failure process of the anchorage interface element is obtained

$$\frac{d^2\delta(x)}{dx^2} = \begin{cases} \alpha^2\delta(x) & 0 \leqslant \delta(x) \leqslant \delta_s^d \\ -\beta^2\delta(x) + \dfrac{2\left(\tau_s^d - K_{AB}\delta_s^d\right)}{r_b E_b} & \delta_s^d \leqslant \delta(x) \leqslant \delta_s^s \\ \dfrac{2\tau_s^s}{r_b E_b} & \delta_s^s \leqslant \delta(x) \end{cases} \tag{2.4}$$

where $\alpha^2 = (2K_{OA})/(r_b E_b)$, $\beta^2 = -(2K_{AB})/(r_b E_b)$.

2.3. Calculation formulas for shear stress and axial force distribution at the anchorage interface

Under the action of axial tensile load, the anchorage interface element will sequentially experience elastic, bond damage, and frictional slip stages. As shown in Fig. 3, the anchorage interface is composed of anchorage interface elements. Therefore, the state of the anchorage interface is determined by the stages in which all interface elements are located. When the anchorage interface elements are in different stages, the anchorage interface will have a situation where parts of the elastic segment, bond damage segment, and frictional slip segment coexist.

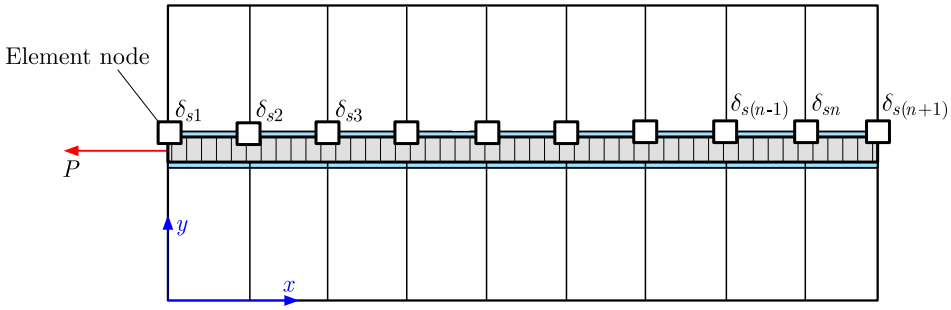

Fig. 3. Schematic diagram of the anchorage interface and interface element relationship

Depending on the state of the anchorage interface elements, the anchorage interface may exist in a full-length elastic stage, elastic-damage stage, full-length damage stage, elastic-damage-slip stage, damage-slip stage, or full-length slip stage. By using the boundary conditions of different stages, combined with Eqs. $(2.2)_1$ and $(2.2)_2$, by solving the load transfer differential equation as shown in Eq. (2.4), it is possible to theoretically calculate the evolution formulas for the distribution of shear stress and axial force along the anchorage interface at different anchorage lengths, as listed in Table 1.

3. Anchor rod pull-out tests

3.1. Preparation of anchorage specimens and test scheme

The evolution law of stress distribution at the anchorage interface is closely related to the parameters of the interface element constitutive model. To determine the model parameters of the anchorage interface and to explore the influence of different anchoring agents on the support effect of the anchor rod, three groups of anchor rod pull-out tests were designed. The tests used large cylindrical specimens made of C40 concrete with a diameter of $d_r = 300\,\text{mm}$ and a length of $l_r = 600\,\text{mm}$ to simulate the anchoring matrix. During preparation of the anchoring matrix, a pipe with an outer diameter of $d_a = 30\,\text{mm}$ was inserted into the center of the

Table 1. Formulas for shear stress and axial force distribution at the anchorage interface in different stages

Anchorage interface stage	Boundary conditions	Distribution formulas of interfacial shear stress and rockbolt axial force
Full-length elastic stage	$P(x)\|_{x=0} = P_0$ $P(x)\|_{x=L} = 0$	$\tau(x) = \frac{\alpha P_0 \cosh[\alpha(L-x)]}{2\pi r_b \sinh(\alpha L)} \quad 0 \leqslant x \leqslant L$ $P(x) = \frac{P_0 \sinh[\alpha(L-x)]}{\sinh(\alpha L)} \quad 0 \leqslant x \leqslant L$
Elastic--damage stage	$P_e(x)\|_{x=L} = 0$ $\tau_e(x)\|_{x=l_d} = \tau_s^d$ $\tau_d(x)\|_{x=l_d} = \tau_s^d$ $P_d(x)\|_{x=l_d}$ $= P_e(x)\|_{x=l_d}$	$\tau(x) = \begin{cases} \tau_s^d \cos[\beta(l_d - x)] \\ \quad -\frac{\beta\tau_s^d}{\alpha}\tanh[\alpha(L-l_d)]\sin[\beta(l_d-x)] \\ \quad 0 \leqslant x \leqslant l_d \\ \frac{\tau_s^d \cosh[\alpha(L-x)]}{\cosh[\alpha(L-l_d)]} \quad l_d \leqslant x \leqslant L \end{cases}$ $P(x) = \begin{cases} 2\pi r_b \tau_s^d \{\frac{\tanh[\alpha(L-l_d)]\cos[\beta(l_d-x)]}{\alpha} \\ \quad +\frac{\sin[\beta(l_d-x)]}{\beta}\} \quad 0 \leqslant x \leqslant l_d \\ \frac{2\pi r_b \tau_s^d \sinh[\alpha(L-x)]}{\alpha\cosh[\alpha(L-l_d)]} \quad l_d \leqslant x \leqslant L \end{cases}$
Full-length damage stage	$P(x)\|_{x=0} = P_0$ $P(x)\|_{x=L} = 0$	$\tau(x) = \frac{\beta P_0 \cos[\beta(L-x)]}{2\pi r_b \sin(\beta L)} \quad 0 \leqslant x \leqslant L$ $P(x) = \frac{P_0 \sin[\beta(L-x)]}{\sin(\beta L)} \quad 0 \leqslant x \leqslant L$
Elastic--damage--slip stage	$\tau_e(x)\|_{x=l_d+l_f} = \tau_s^d$ $P_e(x)\|_{x=L} = 0$ $\tau_d(x)\|_{x=l_d+l_f} = \tau_s^d$ $\tau_d(x)\|_{x=l_f} = \tau_s^s$ $P_d(x)\|_{x=l_d+l_f}$ $= P_e(x)\|_{x=l_d+l_f}$	$\tau(x) = \begin{cases} \tau_s^s \quad 0 \leqslant x \leqslant l_f \\ \frac{\tau_s^s \sin[\beta(l_d+l_f-x)] - \tau_s^d \sin[\beta(l_f-x)]}{\sin(\beta l_d)} \\ \quad l_f \leqslant x \leqslant l_f + l_d \\ \frac{\tau_s^d \cosh[\alpha(L-x)]}{\cosh[\alpha(L-l_d-l_f)]} \quad l_f + l_d \leqslant x \leqslant L \end{cases}$ $P(x) = \begin{cases} 2\pi r_b \tau_s^d \{\frac{\sin(\beta l_d)}{\beta} + \frac{\tanh[\alpha(L-l_d-l_f)]\cos(\beta l_d)}{\alpha}\} \\ \quad +2\pi r_b \tau_s^s (l_f - x) \quad 0 \leqslant x \leqslant l_f \\ 2\pi r_b \tau_s^d \{\frac{\tanh[\alpha(L-l_d-l_f)]\cos[\beta(l_d+l_f-x)]}{\alpha} \\ \quad +\frac{\sin[\beta(l_d+l_f-x)]}{\beta}\} \quad l_f \leqslant x \leqslant l_f + l_d \\ \frac{2\pi r_b \tau_s^d \sinh[\alpha(L-x)]}{\alpha\cosh[\alpha(L-l_d-l_f)]} \quad l_f + l_d \leqslant x \leqslant L \end{cases}$
Damage--slip stage	$P_d(x)\|_{x=L} = 0$ $\tau_d(x)\|_{x=l_f} = \tau_s^s$ $P_f(x)\|_{x=l_f}$ $= P_d(x)\|_{x=l_f}$ $\delta_f(x)\|_{x=l_f} = \delta_s^s$	$\tau(x) = \begin{cases} \tau_s^s \quad 0 \leqslant x \leqslant l_f \\ \frac{\tau_s^s \cos[\beta(L-x)]}{\cos[\beta(L-l_f)]} \quad l_f \leqslant x \leqslant L \end{cases}$ $P(x) = \begin{cases} 2\pi r_b \tau_s^s \{l_f - x + \frac{\tan[\beta(L-l_f)]}{\beta}\} \quad 0 \leqslant x \leqslant l_f \\ \frac{2\pi r_b \tau_s^s \sin[\beta(L-x)]}{\beta\cos[\beta(L-l_f)]} \quad l_f \leqslant x \leqslant L \end{cases}$
Full-length slip stage	–	$\tau(x) = \tau_s^s \quad 0 < x < L$ $P(x) = P_0 - 2\pi r_b \tau_s^s x \quad 0 \leqslant x \leqslant L$

Note: l_d is the length of the bond damage segment, l_f is the length of the slip segment.

anchoring matrix preparation mold to prefabricate the anchoring borehole. The anchor rod used for anchoring was a left-handed thread steel anchor rod with a model number of MG400 and an equivalent diameter of $d_b = 20\,\text{mm}$. The elastic modulus of the anchor rod was $E_b = 200\,\text{GPa}$, the yield load $P_y = 150\,\text{kN}$, and the breaking load $P_f = 210\,\text{kN}$.

Three different types of anchoring agents were selected for the tests: resin anchoring agent, cement grout with a water-cement ratio of 0.45:1, and cement mortar with a water-cement-sand ratio of 0.45:1:1. The designed length of the anchorage section is $l_a = 200\,\text{mm}$, and the calculation formula for the required volume of anchoring agent is

$$V = \frac{\pi}{4} l_a (d_a^2 - d_b^2) \tag{3.1}$$

According to Eq. (3.1), the volume of anchoring agent required for an anchorage length of 200 mm is calculated to be $V = 78.5\,\text{cm}^3$. After injecting the anchoring material, the anchor

rods are inserted for anchoring, and the tests are conducted after 7 days of curing. Figure 4 shows the three groups of anchoring samples prepared in the laboratory.

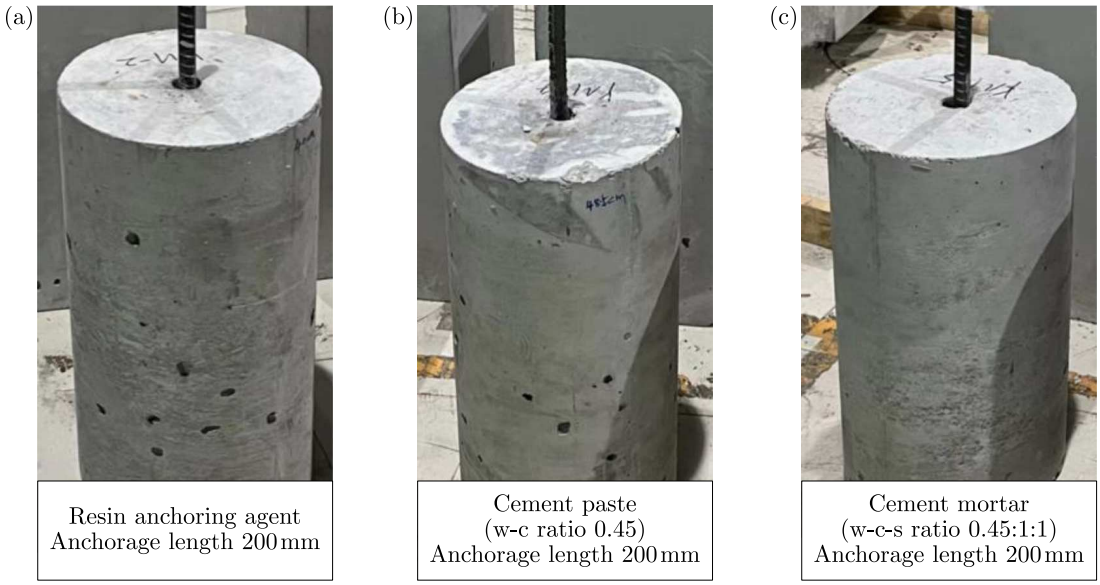

Fig. 4. Diagram of three groups of anchorage specimens prepared in the laboratory

Fig. 5. The RTR-3122 full-scale anchorage performance tester

The anchor rod pull-out tests are conducted on the self-developed RTR-3122 model full-scale anchor rod anchorage performance testing machine (as shown in Fig. 5). Before the test, an anchorage pull-out device is installed on the anchorage performance testing machine. One end of the anchorage specimen is blocked by a rigid load-bearing plate and suspended behind the stop plate of the testing machine. The stop plate serves to fix the anchorage specimen and also prevents wedge failure of the rock mass during the pull-out process. The loading end applies a displacement loading by clamping the free end of the anchor rod with the wedge-shaped clamp of the testing machine. An LVDT (linear variable differential transformer) fixed frame is installed at a measuring point 200 mm away from the rock mass stop plate on the free section of the anchor

rod. The spring probe of the LVDT displacement sensor is placed at the stop plate to record the relative displacement between the anchor rod measuring point and the rock mass, as shown in Fig. 6.

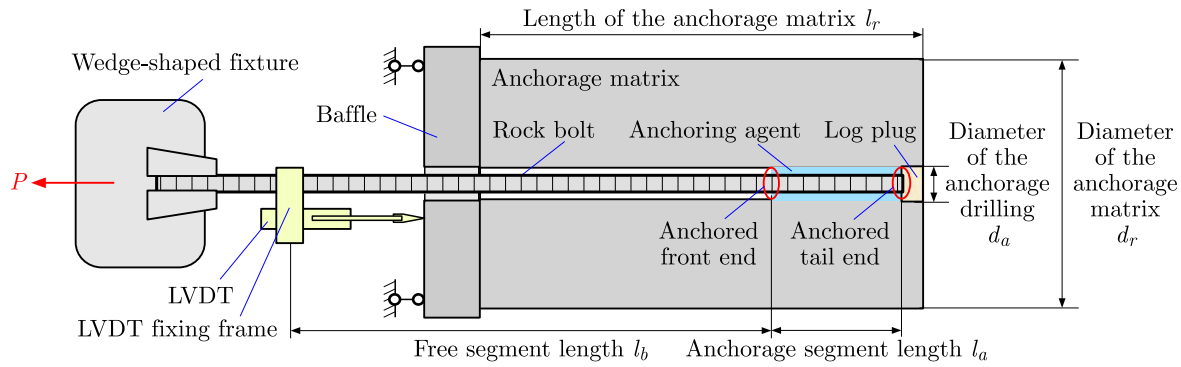

Fig. 6. Schematic diagram of the anchor rod pull-out tests

3.2. Mechanical characteristic curves of the anchorage interface and constitutive model parameters

The tests obtained the axial tensile load-displacement curves of short anchor rods under the action of different anchoring agents (P-δ_{s0} curves), as shown in Fig. 7. The peak tensile loads of the anchor rods under the three test conditions are all less than the yield load of the anchor rod, indicating that the anchor rods were pulled out in the elastic stage.

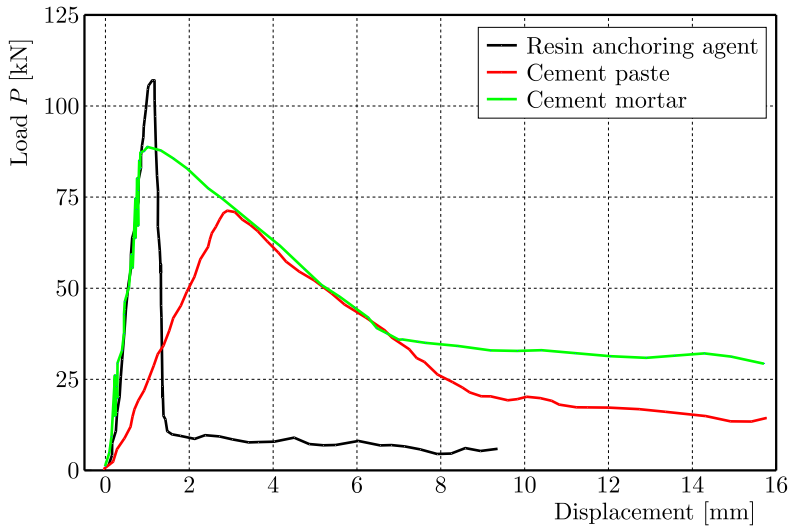

Fig. 7. Anchorage pull-out load-displacement curves

Since the LVDT displacement meter is fixed between the anchor rod and the testing machine stop plate, the measured displacement δ_{s0} is the displacement of the anchor rod measuring point relative to the stop plate, which includes both the elastic deformation of the free section of the anchor rod and the relative displacement between the anchor rod and the rock mass. Subtracting the elastic deformation of the free section of the anchor rod from δ_{s0} allows us to obtain the relative displacement between the anchor rod and the rock mass, i.e., the shear displacement of the anchor rod-rock mass coupling interface. The calculation formula is

$$\delta_s = \delta_{s0} - \frac{4Pl_b}{\pi d_b^2 E_b} \tag{3.2}$$

where l_b represents the length of the free section of the anchor rod.

Since the anchorage section length designed in the test is relatively short, it can be assumed that the shear stress at the anchorage interface is uniformly distributed. Based on the anchor rod pull-out load-displacement curve, the calculation formula for the shear stress τ_s at the anchor rod-rock mass coupling interface is

$$\tau_s = \frac{P}{\pi d_b l_a} \tag{3.3}$$

where l_a represents the length of the anchorage section.

Since the anchor rod does not yield during short anchorage pull-out, the test curve can be considered as the mechanical characteristic curve of a single anchorage interface element. Based on the shear stress-shear displacement relationship curve, the interface model parameters shown in Fig. 1 can be calibrated, where the calculation formulas for τ_s^d and τ_s^s are as follows

$$\tau_s^d = \frac{P_{max}}{\pi d_b l_a} \qquad \tau_s^s = \frac{P_{res}}{\pi d_b l_a} \tag{3.4}$$

where P_{max} is the peak tensile load in the elastic stage of axial stretching of the anchor rod, P_{res} is the residual tensile load in the axial stretching of the anchor rod.

The shear stress-shear displacement relationship curves of the anchor rod-rock mass coupling interface, calculated under different anchoring agent conditions according to Eqs. (3.2) to (3.3), are shown in Fig. 8. The constitutive model parameters of the anchorage interface element under the action of different anchoring agents are calculated and obtained, as listed in Table 2.

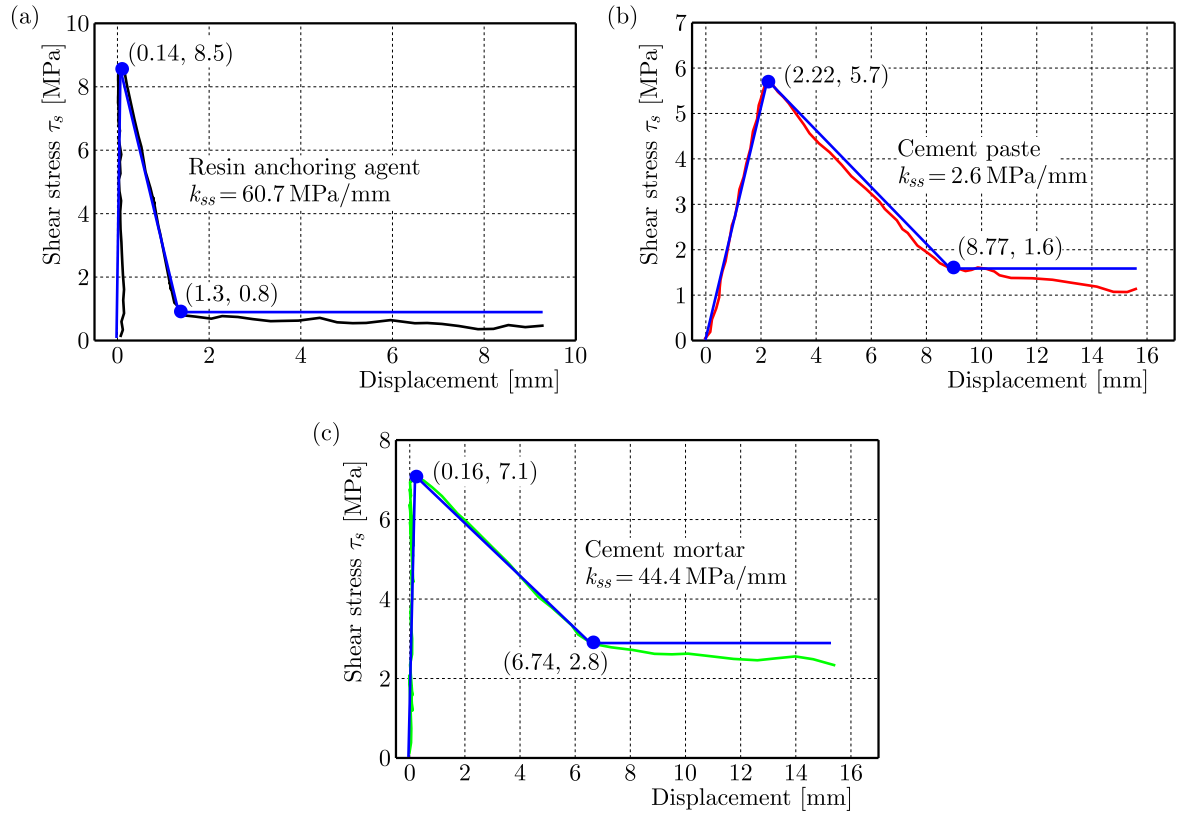

Fig. 8. Anchorage interface mechanical characteristic curves: (a) resin anchoring agent, (b) cement paste, (c) cement mortar

From Fig. 8, it can be seen that different anchoring agents have a significant impact on the mechanical parameters characterizing the bonding performance of the anchorage interface. Under the action of different anchoring agents, the ranking of the peak shear strength of the anchorage

Table 2. Trilinear bond-slip constitutive model parameters under different anchorage agent conditions

Anchoring agent types	τ_s^d [MPa]	δ_s^d [mm]	τ_s^s [MPa]	δ_s^s [mm]	k_{SS} [MPa/mm]
Resin anchoring agent	8.5	0.14	0.8	1.3	60.7
Cement paste	5.7	2.22	1.6	8.77	2.6
Cement mortar	7.1	0.16	2.8	6.74	44.4

interface is: resin anchoring agent > cement mortar > cement paste; the ranking of the residual shear strength of the anchorage interface is: cement mortar > cement paste > resin anchoring agent; the ranking of the residual shear displacement of the anchorage interface is: cement paste > cement mortar > resin anchoring agent; the elastic shear stiffness of the anchorage interface varies greatly, with the highest reaching 60.7 MPa/mm and the lowest being 2.6 MPa/mm, and the ranking is: resin anchoring agent > cement mortar > cement paste. Comparing Fig. 8b and Fig. 8c, it can be seen that when cement is used as the anchoring agent, adding sand particles to the anchoring agent can increase the peak shear strength, residual shear strength, and elastic shear stiffness of the anchorage interface, but at the same time, it reduces the initial sliding displacement of the anchorage interface.

3.3. Load transfer laws of the anchorage interface under the action of different anchoring agents

Assuming the anchorage length $L = 600$ mm, based on the constitutive model parameters of the anchorage interface element shown in Fig. 8, and using the evolution formulas for the distribution of shear stress and axial force at the anchorage interface listed in Table 1, theoretical calculations can be made to obtain the distribution and evolution process of the shear stress and axial force during the entire process of interface debonding failure under different anchoring agent conditions, as shown in Fig. 9.

Since the anchor rod itself has a certain bearing limit, when the theoretical calculated axial force exceeds the breaking load of the anchor rod, the anchor rod will break. The breaking load P_b of the anchor rod used in the test is 210 kN. From Fig. 9, it can be seen that when the anchorage length is 600 mm, the anchor body under the conditions of resin anchoring agent and cement mortar anchoring will experience anchor rod breakage failure, while under the condition of cement grout anchoring, the anchor body will experience interface debonding slip failure. Observing the distribution of interface shear stress when the axial force equals the breaking load of the anchor rod in Figs. 9a and 9e, it is shown that the anchor rod will break in the elastic-damage stage of the anchorage interface. At that moment, the degree of damage to the anchorage interface is relatively low, indicating that the anchorage support effect is greatly influenced by the strength limit of the anchor rod at this time. Observing Figs. 9a, 9c, and 9e, it can be seen from the distribution pattern of shear stress in different sections of the anchorage interface that the greater the elastic shear stiffness k_{ss} of the interface, the more obvious the decay of the shear stress and axial force in the elastic section of the interface along the anchorage length, and the smaller the axial force of the anchor rod when the interface begins to damage.

4. Analysis of the bearing performance of the anchorage interface

4.1. Theoretical analysis of the ultimate bearing capacity of the anchorage interface

Based on the theoretical analysis mentioned above, with the known breaking load of the anchor rod, the ultimate anchorage force of the anchorage interface can be calculated theoreti-

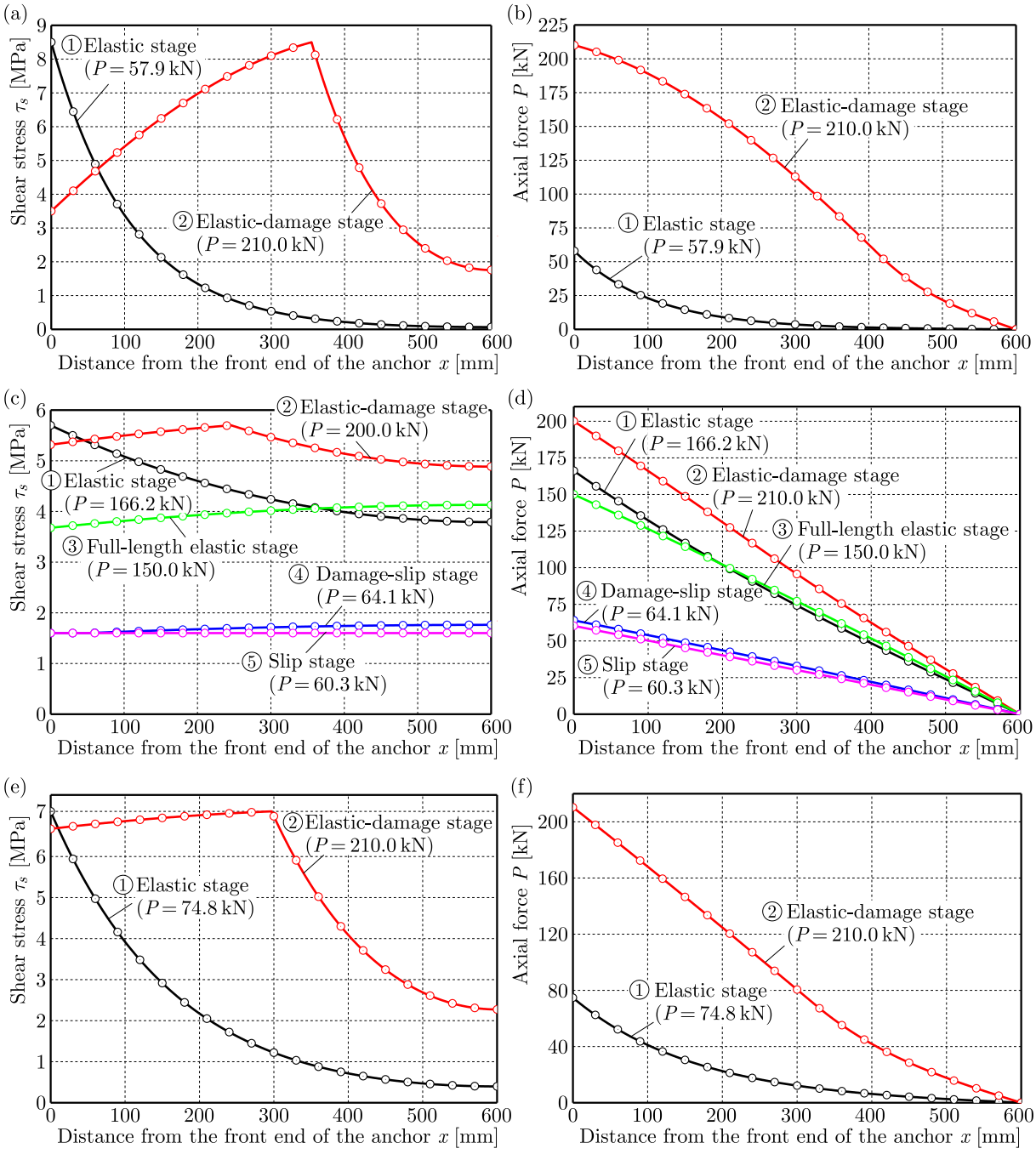

Fig. 9. Distribution curves of the shear stress and axial force under different anchorage agent conditions with anchorage length of 600 mm: (a)–(b) resin anchoring agent, (c)–(d) cement paste, (e)–(f) cement mortar

cally. According to the constitutive model parameters of the anchorage interface calibrated with different test data as shown in Fig. 8, using the aforementioned theoretical calculation method, the curve of the interface ultimate anchorage force changing with the anchorage length under different anchoring agent conditions can be calculated, as shown in Fig. 10. It can be seen from the figure that the relationship between the ultimate anchorage force of the anchorage interface and the anchorage length is related to the interface model parameters. Under the condition of resin anchoring agent, the ultimate anchorage force tends to approach a certain fixed value as the

anchorage length increases. Under the conditions of cement grout and cement mortar anchoring, the ultimate anchorage force increases approximately linearly with the anchorage length.

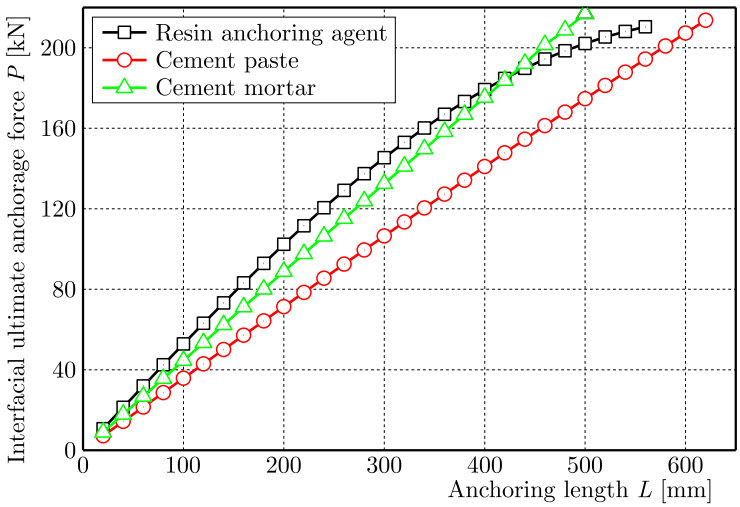

Fig. 10. Variation curves of interfacial ultimate anchorage force with anchorage length

At the same anchorage length, the interface ultimate anchorage force is generally smaller under the condition of cement grout anchoring; when the anchorage length is less than 420 mm, the interface ultimate anchorage force under the condition of resin anchoring agent is greater than that of cement mortar and cement grout anchoring at the same anchorage length. When the anchorage length is greater than 420 mm, the interface ultimate anchorage force with cement mortar is greater than that with resin anchoring agent at the same anchorage length. This indicates that when the anchorage length is relatively small, the magnitude of the interface ultimate anchorage force is determined by the bonding strength, and the greater the peak shear strength, the greater the interface ultimate anchorage force. However, when the anchorage length is relatively large, the contribution of residual stage friction to improving the interface bearing capacity increases, and at this time, the greater the residual shear strength, the greater the interface ultimate anchorage force.

4.2. Experimental verification of the ultimate bearing capacity of the anchorage interface

To verify the accuracy of the theoretical calculation results of the ultimate anchorage force of the anchorage interface, cement grout with a water-cement ratio of 0.45:1m was used as the anchoring agent. The anchor rod pull-out test scheme shown in Fig. 6 was adopted to conduct anchor rod tensile tests on anchor bodies with anchorage lengths of 300 mm, 400 mm, 500 mm, and 600 mm. The tensile load-displacement curves obtained from the test are shown in Fig. 11. The experimental and theoretical values of the ultimate anchorage force at different anchorage lengths, as well as the theoretical deviation rates, are listed in Table 3. The deviation rates are relatively small, indicating a high degree of conformity between the experimental and theoretical values. When the anchorage length is 500 mm and 600 mm, the anchor rod yields during the tensile process, and the experimental value of the interface ultimate anchorage force is less than the theoretically calculated value, with a theoretical deviation rate reaching 3.0%. This indicates that the yield strengthening of the anchor rod will lead to reduction in the bearing capacity of the anchorage interface.

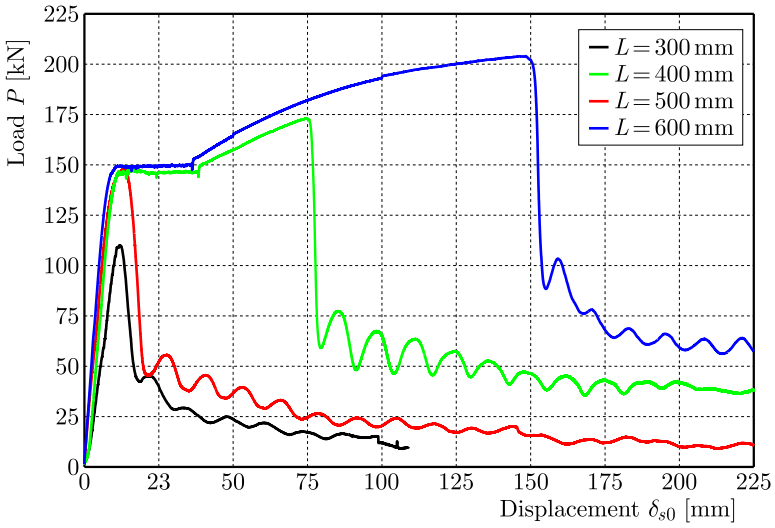

Fig. 11. Load-displacement curves with different anchorage lengths under the cement paste anchorage condition

Table 3. Experimental and theoretical values of the interfacial ultimate anchorage force

Anchorage length L [mm]	Experimental values [kN]	Theoretical values [kN]	Deviation rate of theoretical values [%]
300	108	107	−0.9
400	144	141	−2.1
500	170	175	2.9
600	201	207	3.0

5. Conclusions

(1) Based on the three-stage model, a constitutive equation for the evolution of shear stress damage in the anchorage interface element was established, and theoretical derivations were obtained for the expressions of shear stress and axial force distribution evolution at the anchorage interface during the entire process of anchor rod pull-out.

(2) Anchor rod pull-out tests were conducted to provide a method for calibrating the interface model parameters. Different anchoring agents have a significant impact on the interface model parameters. Compared with cement grout and cement mortar, applying the resin anchoring agent, the interface peak shear strength is larger, but the initial slip displacement and friction force during the slip stage are the smallest.

(3) The load transfer laws and bearing performance of the anchorage interface under the action of different anchoring agents were calculated and analyzed. Since the anchor rod has a certain bearing limit, when the theoretical calculated axial force exceeds the breaking load of the anchor rod, the anchor rod will fail by breaking. Therefore, the theoretical calculation and analysis method can predict the mode of anchorage failure. The greater the elastic shear stiffness of the anchorage interface, the more obvious the decay of shear stress and axial force in the elastic section of the interface along the anchorage length, and the smaller the axial force of the anchor rod when the interface begins to damage.

(4) The ultimate anchorage force of the interface at different anchorage lengths can be obtained through theoretical calculations. The test validation results show that the error between the experimental and theoretical value of the interface ultimate anchorage force is within 3%.

However, the yield strengthening of the anchor rod will reduce the anchorage bearing capacity, and the error of the theoretical calculation value will increase.

Acknowledgement

This research was supported by Taishan Scholar in Shandong Province of China (Grant No. tstp20221126), and the National Natural Science Foundation of China (Grant Nos. 52374097 and 52104137). The authors of this article are very grateful for the support provided.

References

1. Cai Y., Esaki T., Jiang Y.J., 2004, A rock bolt and rock mass interaction model, *International Journal of Rock Mechanics and Mining Sciences*, **41**, 7, 1055-1067
2. Cao C., Ren T., Cook C., 2014, Introducing aggregate into grouting material and its influence on load transfer of the rockbolting system, *International Journal of Mining Science and Technology*, **24**, 3, 325-328
3. Chen J.H., He F.L., Zhang S.B., 2020, A study of the load transfer behavior of fully grouted rock bolts with analytical modelling, *International Journal of Mining Science and Technology*, **30**, 1, 105-109
4. Chen J.H., Li D.Q., 2022, Numerical simulation of fully encapsulated rock bolts with a tri-linear constitutive relation, *Tunnelling and Underground Space Technology*, **120**, 104265.
5. Chen J.H., Liu P., Zhao H.B., Zhang C., Zhang J., 2021, Analytical studying the axial performance of fully encapsulated rock bolts, *Engineering Failure Analysis*, **128**, 105580
6. Du Y.L., Feng G.R., Kang H.P., Zhang Y.J., Zhang X.H., 2021, Effects of different pull-out loading rates on mechanical behaviors and acoustic emission responses of fully grouted bolts, *Journal of Central South University*, **28**, 7, 2052-2066
7. Fan J.Q., Shi X.Y., Kong F.L., Guo J.Q., 2021, Calculation method of the effective anchorage length of anchorage structures based on analysis of the ultimate bearing capacity, *Geotechnical and Geological Engineering*, **39**, 6, 4205-4212
8. Holý O., 2017, Evaluation of many load tests of passive rock bolts in the Czech Republic, *Geoscience Engineering*, **63**, 1, 1-7
9. Huang M.H., Zhao M.H., Chen C.F., 2019, Study of the mechanical features of the bolts under tension based on the nonlinear bond-slip model (in Chinese), *Journal of Safety and Environment*, **19**, 4, 1196-1203
10. Høien A.H., Li C.C., Zhang N., 2021, Pull-out and critical embedment length of grouted rebar rock bolts-mechanisms when approaching and reaching the ultimate load, *Rock Mechanics and Rock Engineering*, **54**, 1431-1447
11. Kilic A., Yasar E., Celik A.G., 2002, Effect of grout properties on the pull-out load capacity of fully-grouted rock bolt, *Tunnelling and Underground Space Technology*, **17**, 4, 355-362
12. Li C.C., 2010, Field observations of rock bolts in high stress rock masses, *Rock Mechanics and Rock Engineering*, **43**, 4, 491-496
13. Liu X.H., Yao Z.S., Xue W.P., Wang X.S., Huang X.W., 2021, Experimental study of the failure mechanism of the anchorage interface under different surrounding rock strengths and ambient temperatures, *Advances in Civil Engineering*, **2021**, 1, 622418
14. Ma S.Q., Zhao Z.Y., Nie W., Gui Y.L., 2016, A numerical model of fully grouted bolts considering the tri-linear shear bond–slip model, *Tunnelling and Underground Space Technology*, **54**, 73-80

15. Nemcik J., Ma S.Q., Aziz N., Ren T., Geng X., 2014, Numerical modelling of failure propagation in fully grouted rock bolts subjected to tensile load, *International Journal of Rock Mechanics and Mining Sciences*, **71**, 293-300

16. Nie W., Zhao Z.Y., Guo W., Shang J., Wu C., 2019, Bond-slip modeling of a CMC rock bolt element using 2D-DDA method, *Tunnelling and Underground Space Technology*, **85**, 340-353

17. Wang Y., Li C.D., Cai Z.L., Zhu G.Q., Zhou J.Q., Yao W.M., 2023, Mechanical behaviors of anchorage interfaces in layered rocks with fractures under axial loads, *Journal of Earth Science*, **34**, 2, 354-368

18. Wu Q.H., Chen L., Shen B.T., Dlamini B.G., Li S.Q., Zhu Y.J., 2019, Experimental investigation on rockbolt performance under the tension load, *Rock Mechanics and Rock Engineering*, **52**, 11, 4605-4618

19. Yahia A., Khayat K.H., Benmokrane B., 1998, Evaluation of cement grouts for embedding anchors under water, *Materials and Structures*, **31**, 4, 267-274

20. Yi K., Kang H.P., Ju W.J., Liu Y.D., Lu Z.G., 2020, Synergistic effect of strain softening and dilatancy in deep tunnel analysis, *Tunnelling and Underground Space Technology*, **97**, 103280

21. Yue Z.W., Li A., Wang P., Wang P., 2022, An analytical analysis for the mechanical performance of fully-grouted rockbolts based on the exponential softening model, *International Journal of Mining Science and Technology*, **32**, 5, 981-995

22. Zhao T.B., Xing M.L., Guo W.Y., Wang C.W., Wang B., 2021, Anchoring effect and energy-absorbing support mechanism of large deformation bolt, *Journal of Central South University*, **28**, 2, 572-581

Manuscript received October 2, 2024; accepted for publication December 6, 2024